Mechanically active 3D mesostructures

Integrating piezoelectric materials into complex 3D architectures holds potential for many applications

Jose Vazquez (Imaging Technology Group, Beckman Institute, UIUC) and Xin Ning (Department of Materials Science and Engineering, UIUC)
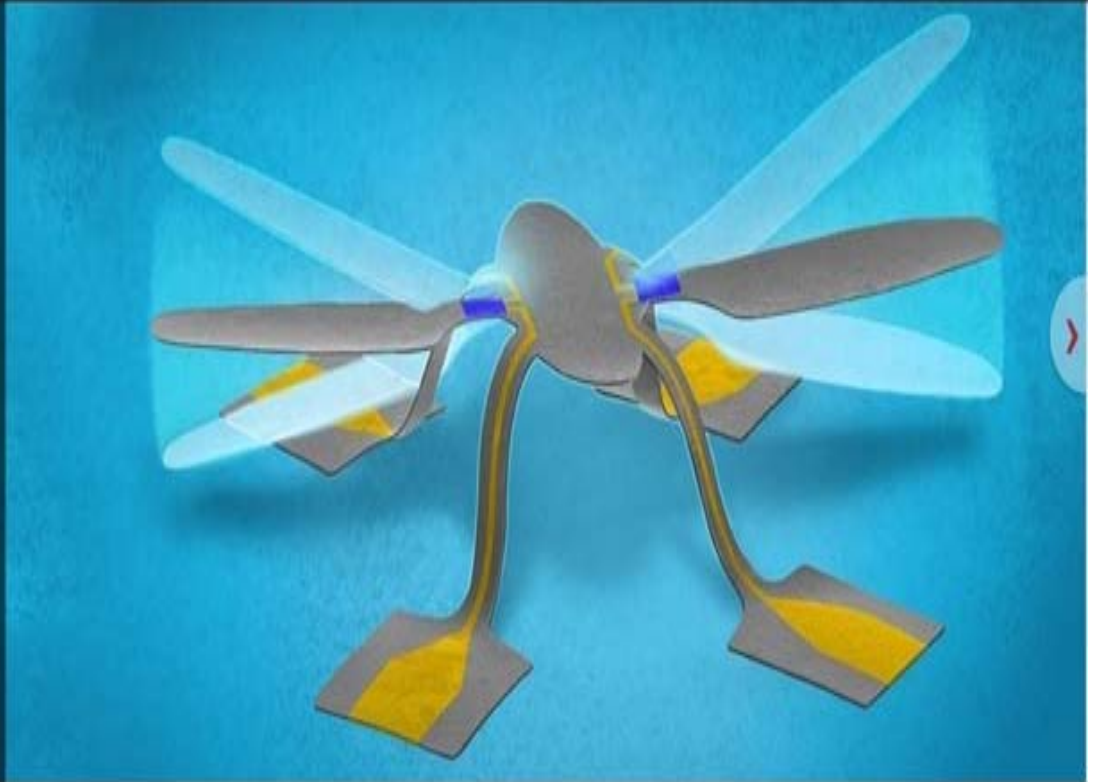
MATERIALS SCIENCE

Mechanically active materials in three-dimensional mesostructures

Xin Ning[1]*, Xinge Yu[2], Heling Wang[3]*, Rujie Sun[4], R. E. Corman[5], Haibo Li[3], Chan Mi Lee[6], Yeguang Xue[3], Aditya Chempakasseril[2], Yao Yao[2], Ziqi Zhang[2], Haiwen Luan[3], Zizheng Wang[2], Wei Xia[7], Xue Feng[8], Randy H. Ewoldt[5], Yonggang Huang[3], Yihui Zhang[8]†, John A. Rogers[1,2,9]†

Complex, three-dimensional (3D) mesostructures that incorporate advanced, mechanically active materials are of broad, growing interest for their potential use in many emerging systems. The technology implications range from precision-sensing microelectromechanical systems, to tissue scaffolds that exploit the principles of mechanobiology, to mechanical energy harvesters that support broad bandwidth operation. The work presented here introduces strategies in guided assembly and heterogeneous materials integration as routes to complex, 3D microscale mechanical frameworks that incorporate multiple, independently addressable piezoelectric thin-film actuators for vibratory excitation and precise control. The approach combines transfer printing as a scheme for materials integration with structural buckling as a means for 2D-to-3D geometric transformation, for designs that range from simple, symmetric layouts to complex, hierarchical configurations, on planar or curvilinear surfaces. Systematic experimental and computational studies reveal the underlying characteristics and capabilities, including selective excitation of targeted vibrational modes for simultaneous measurements of viscosity and density of surrounding fluids. The results serve as the foundations for unusual classes of mechanically active 3D mesostructures with unique functions relevant to biosensing, mechanobiology, energy harvesting, and others.

INTRODUCTION

Microelectromechanical systems (MEMS) have widespread uses in scientific research and in advanced technologies, with prominent examples in accelerometry and inertial guidance, cell mechanics and mechanobiology (1–4), high-precision mass sensing (5, 6), microfluidic control (7, 8) and rheological characterization (9–11), energy harvesting (12–14), and many others. Approaches for forming MEMS leverage manufacturing technologies associated with the semiconductor industry, where two-dimensional (2D) lithographic and etching steps yield mechanical and electrical components in planar, multilayered configurations (15–17). The results typically involve simple 2D collections of mechanically active cantilevers (18), combs (19–21), bridges and wires (22, 23), flat plates, and membranes (24, 25). Extending 2D MEMS into the third dimension expands the range of design options, of broad interest for advanced applications (16, 26–28). The development of schemes for realizing 3D MEMS, especially those that integrate diverse functional materials, represents an active area of research (16, 29, 30). Dynamic actuation is one such function that is critically important for bioMEMS, high-resolution mass sensors, viscometers, radiofrequency

switches and modulators, and others. Piezoelectric materials, especially thin-film piezoelectrics, form the basis of actuators that can produce fast switching with linear force and displacement responses at small driving voltages, in compact and lightweight configurations (31–33). The means for deploying such piezoelectric components, monolithically integrated into complex 3D frameworks, is a topic of current work.

The results presented in the following contribute to the field of mechanically active 3D MEMS through the introduction of routes to complex 3D mesoscale architectures with integrated piezoelectric actuators, each under independent electrical control for dynamic excitation of selected vibrational modes. Here, advanced methods in transfer printing enable integration of ultrathin piezoelectric films and ductile metals onto polymer layers, lithographically patterned into 2D geometries. Controlled processes of mechanical buckling then transform these 2D multifunctional material structures into well-defined 3D architectures (34–38), capable of deployment onto flat or curved surfaces of different classes of substrates. Finite element modeling of the 3D mechanical responses enables selection of structural topologies and of actuator locations for controlled dynamics with engineered distributions of displacements. Experimental, theoretical, and numerical investigations of vibrational actuation in air and in various liquids illustrate the key features. The approach presented here enables active platforms that can serve as devices for measuring viscosity and density of sample-limited volumes of biological fluids, where tailored vibrational modes enable separate determination of dynamic viscosity and density.

RESULTS

Design and assembly of active 3D mechanical mesostructures

Fabrication begins with the formation of 2D precursor structures that integrate multiple functional materials and components via processes in microfabrication and transfer printing. Figure 1A shows a schematic illustration of a precursor and corresponding 3D structure. Figure 1C presents an exploded view of a selected area. The system consists of a photodefinable epoxy framework (SU-8, MicroChem), with patterned

[1]Department of Materials Science and Engineering, Frederick Seitz Materials Research Laboratory, University of Illinois at Urbana-Champaign, Urbana, IL 61801, USA. [2]Simpson Querrey Institute and Feinberg Medical School, Center for Bio-Integrated Electronics, Northwestern University, Evanston, IL 60208, USA. [3]Departments of Civil and Environmental Engineering and Mechanical Engineering, Northwestern University, Evanston, IL 60208, USA. [4]Advanced Composites Centre for Innovation and Science, University of Bristol, Bristol BS8 1TR, UK. [5]Department of Mechanical Science and Engineering, University of Illinois at Urbana-Champaign, Urbana, IL 61801, USA. [6]Department of Chemistry, University of Illinois at Urbana-Champaign, Urbana, IL 61801, USA. [7]State Key Laboratory for Strength and Vibration of Mechanical Structures, Xi'an Jiaotong University, Xi'an, Shaanxi 710049, China. [8]Center for Mechanics and Materials, Center for Flexible Electronics Technology, and Applied Mechanics Laboratory, Department of Engineering Mechanics, Tsinghua University, Beijing 100084, China. [9]Department of Materials Science and Engineering, Biomedical Engineering, Neurological Surgery, Chemistry, Mechanical Engineering, Electrical Engineering and Computer Science, Northwestern University, Evanston, IL 60208, USA.
*These authors contributed equally to this work.
†Corresponding author. Email: jrogers@northwestern.edu (J.A.R.); yihuizhang@tsinghua.edu.cn (Y.Z.)
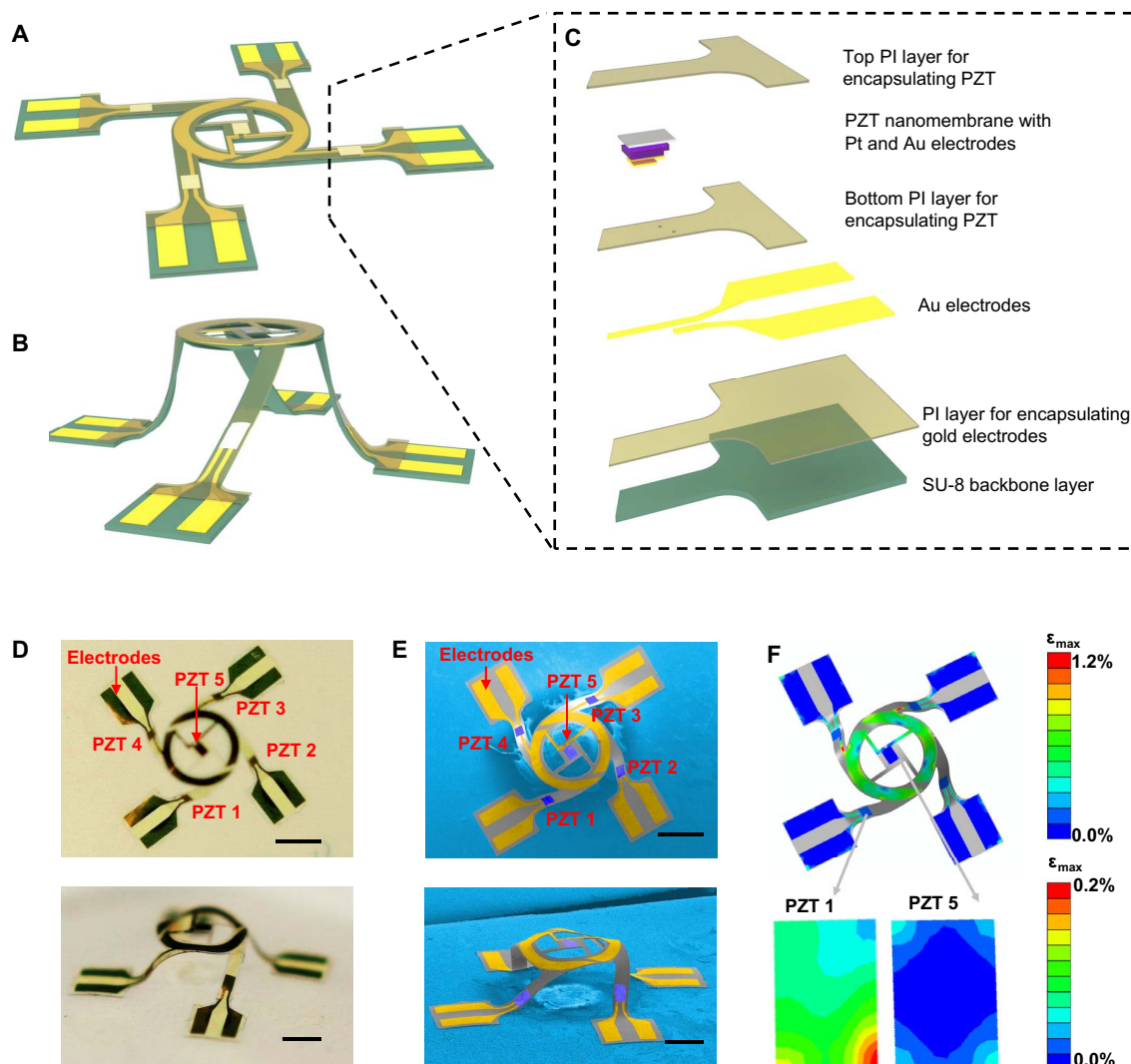
Fig. 1. Schematic illustrations, optical images, SEM images, and finite element modeling results for a representative 3D mesostructure with five independently addressable PZT microactuators. (**A**) Schematic illustration of the 2D architecture of the system. (**B**) Schematic illustration of the 3D system after assembly by controlled biaxial compressive buckling. (**C**) Exploded view of the layout. (**D**) Optical images (top and perspective views) of the 3D architecture. (**E**) SEM images (top and perspective views). The false color of the top-view image highlights the electrodes (gold) and PZT actuators (blue). (**F**) Results of finite element modeling, with color representation for the magnitude of the strain. Only small strains appear in the PZT microactuators. Scale bars, 500 μm.

thin films of $Pb(Zr_{0.52}Ti_{0.48})O_3$ (PZT; mechanical actuation) and gold (Au; electrodes and electrical interconnects), and layers of polyimide (PI) that encapsulate the system everywhere except at selected areas. These areas bond the 3D structure to the elastomeric substrate and serve as contact sites for electrical probing. The PZT microactuators (lateral dimension, 200 μm × 140 μm) incorporate patterned multilayer stacks of PZT (500 nm) sandwiched between bottom (Ti/Pt, 5 nm/200 nm) and top (Cr/Au, 10 nm/200 nm) electrodes. Releasing these components from a temporary substrate allows their delivery to a layer of PI (1.5 μm thick; serves both as an adhesive layer and an encapsulation layer) by transfer printing (*39*). A mechanically guided process of compressive buckling transforms the 2D precursor into a final 3D architecture (Fig. 1B) via release of prestrain in an underlying elastomeric substrate. Figure 1 (D and E) presents optical and scanning electron microscopy (SEM) images, respectively, as top and perspective views of a device that includes five independently addressable PZT microactuators, one at the center and four

on the supporting legs. Detailed information appears in Materials and Methods and figs. S1 to S3. Movie S1 shows the buckling procedure.

Quantitative finite element analysis [FEA; see note S1 (*40*) for details] serves as a means to optimize the locations of the PZT and metal layers to ensure integrity during compressive buckling. [The fracture strain of the PZT is only 0.6% (*41*, *42*).] Figure 1F shows that the predicted 3D configuration agrees well with experimental observation. The peak values of maximum principal strain (ε_{max}) in the PZT and metal are ~0.2 and 1.2%, respectively; both values are well below the corresponding limits of material fracture. By studying a representative 3D structure (fig. S4A), further analyses (fig. S4) indicate an approximately linear dependence of ε_{max} on the square root of the compressive strain (ε_{compre}), that is, $\varepsilon_{max} \propto \sqrt{\varepsilon_{compre}}$ (fig. S4B), consistent with previous reports (*35*). Figure S4 (C and D) shows the dependency of ε_{max} on the thickness of the backbone SU-8 layer and the structure in-plane size, respectively. FEAs provide all strains in this paper.

Active mesostructures with diverse 3D geometries

These schemes provide access to diverse classes of unique 3D microscale architectures. Figure 2 presents a broad set of examples, from simple geometries to complex layouts, with various numbers of independently addressable PZT microactuators. Figure 2A shows side and top views of a simple, symmetric bridge structure with two actuators (blue color) and electrodes (gold color). Attachment to the elastomeric substrate occurs at two bonding pads that also serve as sites for electrical connection. Figure 2B presents another symmetric, but more complex, structure in a geometry that resembles an "insect" with two wings and four
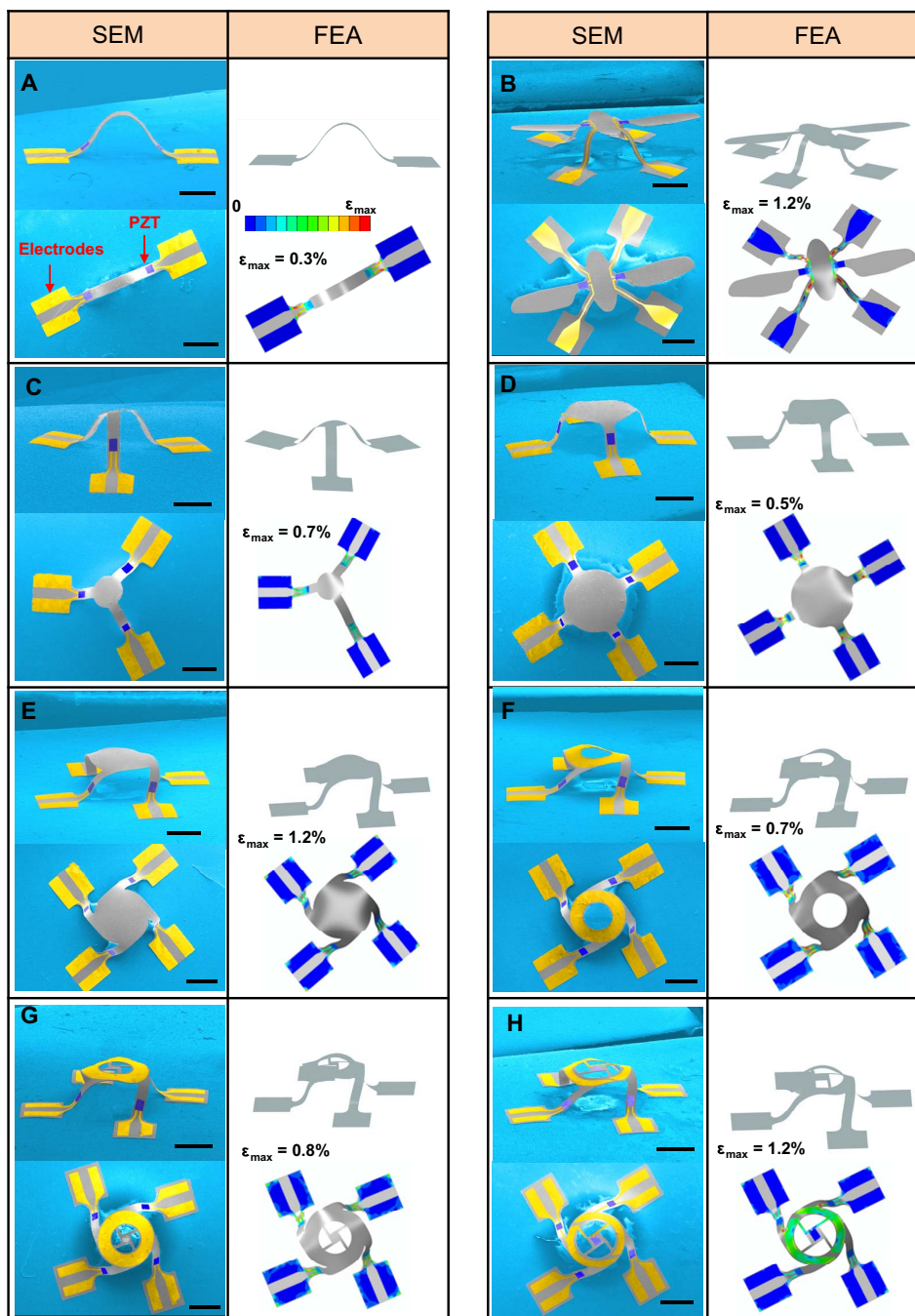

Fig. 2. Demonstration of diverse 3D architectures with integrated PZT microactuators. (**A**) "Bridge" structure with two PZT microactuators. (**B**) "Fly" structure with a pair of actuators on the wings. (**C**) "Tilted pyramid truss" structure with three actuators. (**D**) "Four-leg table" structure with an actuator on each leg. (**E**) "Rotated table" structure with an actuator on each leg. (**F**) "Rotated table" with a central hole on top and four actuators. (**G**) "Double-floor rotated table" structure that consists of a large rotated table and a small one on the top, with four actuators. (**H**) "Double-floor rotated table" structure with five actuators (the additional one on top). Each panel includes a side and a top view. The yellow and blue regions correspond to the electrodes and PZT microactuators, respectively. Scale bars, 500 μm. The contour plots show results of FEA modeling for the maximum principal strain in the electrodes and PZT microactuators.

legs. The PZT layers reside on the wings, and the electrodes travel through the legs to four bonding pads. Asymmetric 3D geometries are also possible, as illustrated with a pyramid truss that incorporates three actuators and legs with different lengths to yield a tilted configuration (Fig. 2C). Figure 2D presents a table structure with ribbon and membrane shapes and four actuators. Variants of this architecture, but with four to five actuators, appear in Fig. 2 (E to H). Figure 2 also summarizes, for each case, geometries computed by FEA. The results exhibit an excellent match with the experimental observations. Further details are in Materials and Methods and note S1. Additional images are in figs. S5 and S6. The geometries of the 2D precursors are in fig. S7. Contour plots in Fig. 2 and fig. S8 present FEA predictions for strains in the PZT, electrode, and SU-8 layers. The peak strain values are below 0.3% (PZT), 1.2% (electrode), and 3.5% (SU-8) and thus below fracture thresholds for all examples. These methods for integrating ultrathin active materials in complex 3D architectures provide access to a wide range of resonant frequencies and diverse vibratory modes that can potentially serve as foundations for 3D MEMS. The following sections include studies on the dynamics of those active mesostructures, as well as demonstrations of their applications in measuring fluid viscosity and density.

Dynamic excitation of selected 3D vibrational modes in air

PZT microactuators strategically placed in regions of specially designed 3D geometries allow deterministic control over the dynamical behavior and resonant modes. Figure 3 presents vibrational responses of representative examples actively excited in this manner. Figure 3A shows the bridge structure and its vibrational behavior excited by its two actuators at various amplitudes. A 180° phase shift between the sinusoidal driving voltages for the two actuators leads to a left-right vibrational direction, as measured using a laser scattering technique (37), in which the amplitude of the observed signal depends linearly on the amplitude of the motion. Details appear in fig. S9. Note that this optical system serves as the basis for all measurements on the structural dynamics presented in this paper. Figure 3A shows that even small driving voltages generate vibrations that can be detected with high signal-to-noise ratio. The resonant frequency, in this case, is 7.7 kHz. Figure 3B presents the normalized dynamical responses, showing that different driving voltages result in the same dynamical behavior. The results in Fig. 3 (B and D) indicate that the structures can be excited with a high repeatability. Figure 3C illustrates the vibrational modes and the dynamic mechanical responses obtained by 3D FEA. Movie S2 summarizes the vibrational modes of all examples in this paper. The predicted resonant frequencies are within 5% of the measured values. FEA predicts that the vibration amplitude is on the order of micrometers at the resonant frequency under a 1-V driving voltage.

The table structure and its two lowest vibrational modes, each excited selectively using timed operation of the PZT microactuators, are in Fig. 3 (D and E). Specifically, operating the two actuators on the left and right legs launches the left-right mode (Fig. 3D); operating the two actuators on the back and front legs launches the back-front mode (Fig. 3E). Because of the symmetry of the structure, these two modes have the same resonant frequencies, confirmed by experiments and FEA simulations. Figure 3F presents the simulated left-right and back-front modes. These results illustrate capabilities in selective modal excitation of 3D structures.

Figure 3G highlights the "insect" structure and its dynamical response. In-phase driving voltages applied to the actuators drive a flapping motion as in Fig. 3H. Experiments and FEA simulations reveal a resonant frequency at 1.15 kHz. Figure 3I shows the dynamic responses of the asymmetric pyramid truss induced by actuating the second-longest leg. Both experiments and FEA simulations identify

a resonant frequency at 10.05 kHz. The corresponding vibrational mode is in Fig. 3J.

The 3D architectures themselves can determine the modal characteristics by virtue of their intrinsic mechanical properties, independent of the actuation method. For example, Fig. 3K presents a double-floor rotated table with a PZT microactuator on each leg, with experimentally determined and simulated dynamic responses. Here, the same driving signal excites all four actuators simultaneously. Figure 3I shows two different resonant modes: a twisting mode at 7.49 kHz and a piston mode at 27.35 kHz. In general, the rotated table and its variants support these types of twisting and piston modes with the same actuation method. Figure S10 presents results for responses of other 3D structures. Additional details are in Materials and Methods and note S1.

According to scaling law analyses (37) of these types of 3D structures, the resonant frequency (f) depends on the material/geometry parameters according to $f \propto \frac{h}{L^2} \sqrt{\frac{\hat{E}}{\rho_{Solid}}}$, where h is the total thickness ($h_{SU-8} + h_{PI}$), L is the in-plane size, $\hat{E}$ is the effective modulus, and ρ_{Solid} is the average density of SU-8 and PI. The PZT and electrode layers can be neglected because of their small in-plane sizes and thicknesses compared with those of the SU-8 and PI. Taking the double-floor rotated table structure (Fig. 3K) as an example, this scaling law agrees well with FEA for 3D structures for a range of different material/geometry parameters (fig. S11), thereby establishing its use in designing systems with desired resonant frequencies of the lowest and second lowest modes.

Separate measurements of viscosity and density using multimodal resonances in optimized 3D mesostructures

The rich range of 3D geometries that can be achieved and the ability to position the PZT microactuators at desired locations provide a large design space for tailoring the excitatory dynamical behaviors to specific application requirements. As a demonstration, Fig. 4 presents experimental, theoretical, and numerical studies on the dynamics of a double-floor rotated table structure (Fig. 2G) tailored for simultaneously measuring viscosity and density of various Newtonian fluids based on two separate resonant modes, which have decoupled sensitivities to fluid viscosity and density, and a theoretical model.

Conventional 2D resonators largely measure the resonant frequency of a single mode, the associated quality factor, or vibratory amplitude and phase to extract the viscosity and/or density (10, 11, 18, 22, 43–50). These measurable parameters are usually sensitive to both viscosity and density in a coupled manner that can complicate their separate determination. Several strategies exist to address this issue. First, data fitting can define the inverse relations between fluid properties and the measurable parameters of a single resonant mode (10, 18, 43, 44, 46). Accurate measurements based on this approach can, however, be difficult. The second approach involves two separate devices with different sensitivities to viscosity and density to bypass this cross-sensitivity issue (48). The third strategy uses multimodal resonances with decoupled sensitivities to viscosity and density (49, 51). Rigorous theoretical models for inversely calculating viscosity and density based on multimodel operation are not well developed. Recent, multimodal resonance strategies can yield the density and modulus of thin films (52). Such approaches have not, however, been extended to measuring viscosity and density of fluids. In addition, accurately measuring the amplitude of high-frequency vibration and quality factors in highly viscous fluids requires sophisticated experimental apparatus (for example, laser Doppler vibrometer) (1) or integrated, precisely calibrated strain sensors (10), leading to further challenges.
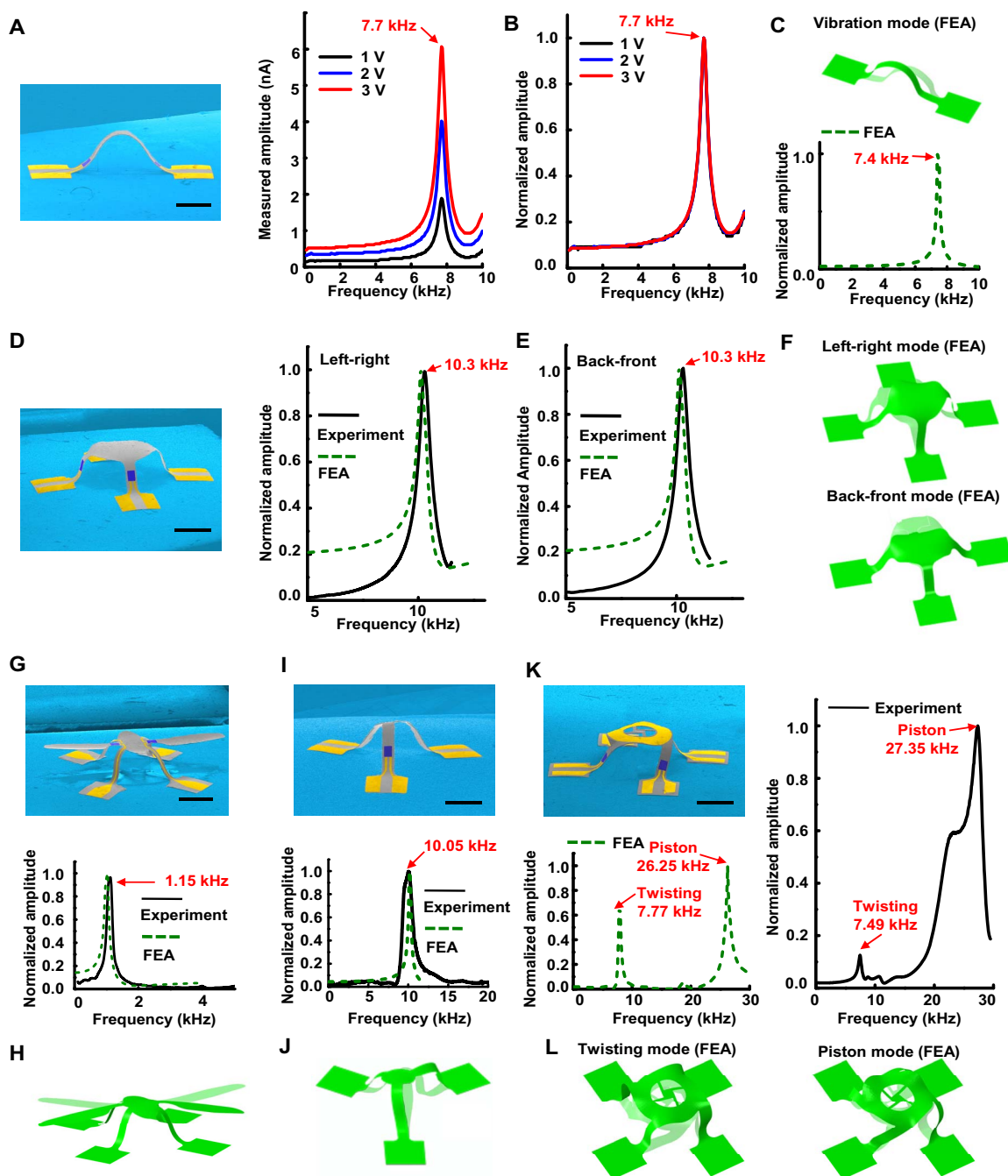
Fig. 3. Vibratory behavior of 3D mesostructures excited by PZT microactuators. (**A**) Bridge structure with two actuators and the experimental amplitude-frequency responses for excitation with different voltages applied to the PZT microactuators. (**B**) Normalized amplitude-frequency curves. (**C**) Finite element modeling of the vibration. (**D** and **E**) Table structure with an actuator integrated on each leg and its amplitude-frequency responses for left-right and back-front vibrational modes. (**F**) Finite element modeling of the resonant modes of the table structure. (**G**) Vibratory responses of the fly structure. (**H**) Flapping mode, selectively excited by integrated actuators. (**I** and **J**) Tilted-pyramid truss dynamic responses and corresponding resonant modes. (**K**) A double-floor rotated table with four actuators and its amplitude-frequency responses. (**L**) The resonant modes of the double-floor rotated table. Scale bars, 500 μm.

Strategic 3D designs enabled by the methods introduced here can yield structures with two qualitatively different and well-separated resonant modes: one corresponding to a twisting motion and the other corresponding to a piston-type vibration (Fig. 3L). The resonant frequencies of these two modes have decoupled sensitivities to viscosity and density, and they serve as the two measurable quantities for simul-

taneous extraction of accurate values of viscosity and density based on a theoretical model. The calculation of viscosity and density does not require the absolute values of vibratory amplitudes or quality factors, significantly reducing the requirements on the measurement system. The device demonstrated here, along with the theoretical model for solving the inverse problem, bypasses many of the issues of alternative
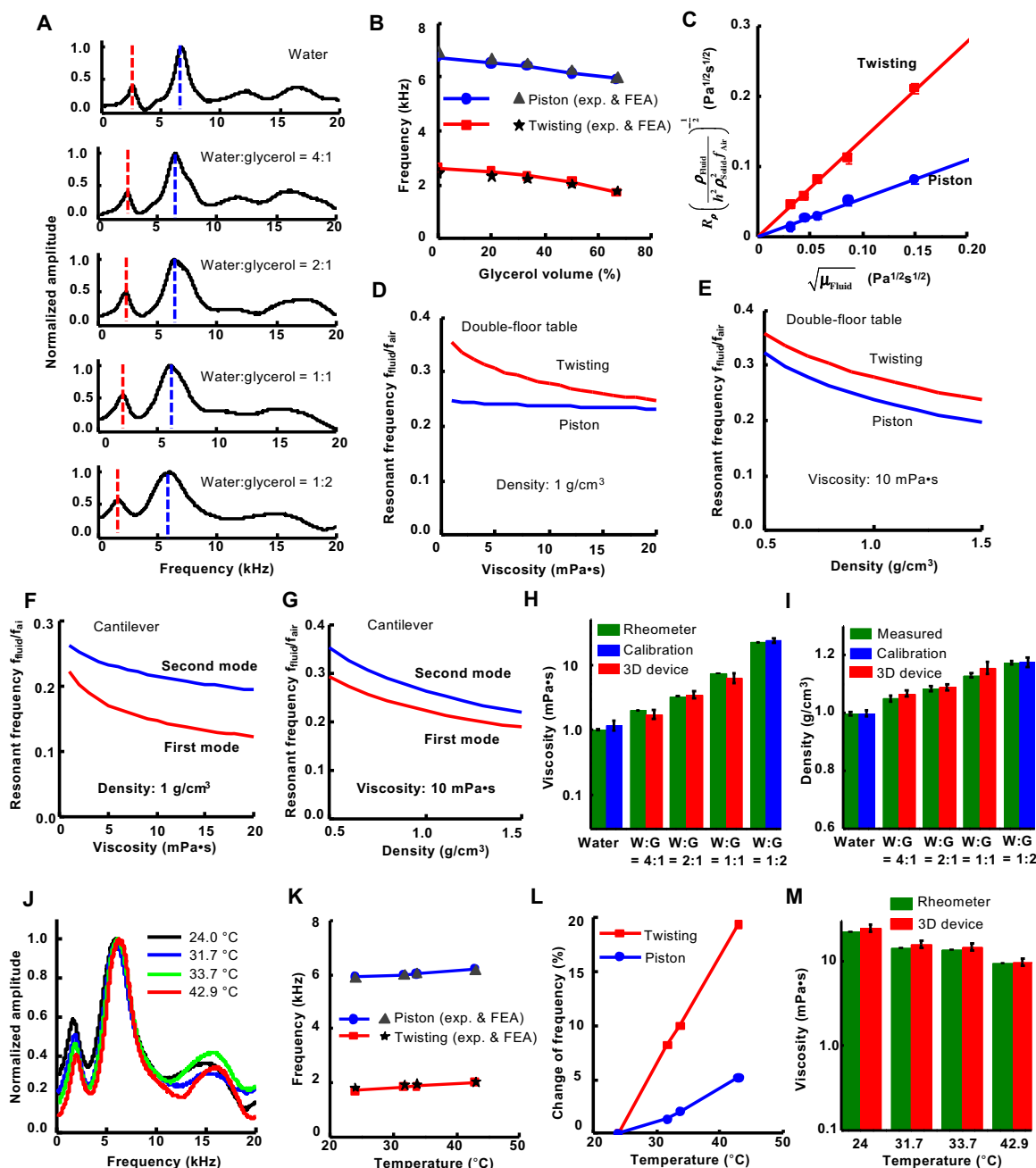
Fig. 4. Strategically optimized 3D mesostructures provide decoupled modes for separate determinations of fluidic density and viscosity. (**A**) Vibratory responses of the double-floor rotated table when immersed in water-glycerol mixtures. (**B**) Change of resonant frequencies as a function of volume fraction of glycerol. (**C**) Theoretical model for the calculation of fluidic properties and its FEA validation. In (C) $R_\rho = \left(\frac{f_{Fluid}}{f_{Air}}\right)^{-\frac{3}{2}} - \left(1 + K\rho \frac{L\rho_{Fluid}}{h\rho_{Solid}}\right)\left(\frac{f_{Fluid}}{f_{Air}}\right)^{-\frac{1}{2}}$. (**D** and **E**) Decoupled sensitivities of the two resonant modes of the double-floor structure to fluidic properties. (**F** and **G**) Coupled sensitivities of a cantilever structure to fluidic properties. (**H** and **I**) Calculated viscosity and density as inferred from theoretical models. (**J**) Measured amplitude-frequency responses at different temperatures. (**K**) Change of resonant frequency as a function of temperature. (**L**) Relative change of resonant frequency as a function of temperature. (**M**) Calculated viscosity at various temperatures. exp., experiment.

approaches and provides a promising alternative to conventional MEMS rheometers.

Figure 4A shows the vibratory responses of the double-floor rotated table structure while immersed in a series of water-glycerol mixtures, where the viscosity ranges from a comparatively low (pure water) to a high (mixture of water and glycerol with a volume ratio of 1:2) value. The first two peaks of the measured response curves correspond to the twisting mode (red dashed line) and the piston mode (blue dashed line).

All experimental frequency-amplitude responses correspond to the average of 64 measurements at each frequency. The SDs at the resonances among the measurements are small (below 5%), indicating that the structures can be excited with a high repeatability in fluids. Figure S12 (A to C) shows the measured dynamics with error bars of the double-floor rotated table structures in water-glycerol mixture (volume ratio of 1:1). Figure 4B presents the resonant frequencies as a function of the volume fraction of glycerol. The frequencies decrease as the volume fraction

of glycerol increases as a consequence of corresponding increases in viscosity. The frequencies obtained from FEA simulations match the experimental results. The response predicted by FEA is in fig. S12 (D and E).

Inspired by the analytical solution of the resonant frequency for a cantilever immersed in inviscid fluid (53), the dependence of the ratio of resonant frequencies in fluid and air, that is, f_{Fluid}/f_{Air}, depends on a dimensionless combination of geometry and densities $L\rho_{Fluid}/(h\rho_{Solid})$, where ρ_{Fluid} and ρ_{Solid} are the fluid density and the average density of the 3D structure, and h and L denote the thickness and the in-plane size of the 3D structure, respectively. This ratio results from a comparison of added inertial mass of the surrounding fluid compared to the inertial mass of the cantilever; each scale differently with geometry leaving the L/h ratio. The Reynolds number $Re = \rho_{Fluid} f L^2 / \mu_{Fluid}$ measures the effect of fluid viscosity on vibration or motion, where f is a characteristic frequency of the vibration (53), and μ_{Fluid} is the fluid viscosity. According to these considerations, a scaling law is proposed as

$$\frac{f_{Fluid}}{f_{Air}} = G\left(\frac{L\rho_{Fluid}}{h\rho_{Solid}}, \frac{\rho_{Fluid} f_{Air} L^2}{\mu_{Fluid}}\right) \quad (1)$$

In general, G is a nonlinear double-variable function depending on the topology of the 3D structure and the vibrational mode. Equation 1 is consistent with coupled simulations of the fluid structure, as shown in fig. S13 and note S2 (53). When the Reynolds number is far larger than 1, the scaling law (Eq. 1) can be simplified to an explicit form by assuming asymptotic effects of Re on the added inertial mass of the surrounding fluid, which can be understood from a viscous momentum diffusion length scale increasing the added mass (see note S3 for details)

$$\left(1 + K_\rho \frac{L\rho_{Fluid}}{h\rho_{Solid}}\right)\left(\frac{f_{Fluid}}{f_{Air}}\right)^2 + K_\mu \left(\frac{\mu_{Fluid}\rho_{Fluid}}{h^2\rho_{Solid}^2 f_{Air}}\right)^{\frac{1}{2}}\left(\frac{f_{Fluid}}{f_{Air}}\right)^{\frac{3}{2}} = 1 \quad (2)$$

where K_ρ and K_μ are two constants that depend on the topology of the structure and the vibrational mode, associated with leading-order added mass of the fluid, and Re modification to added mass, respectively. For the double-floor rotated table structure shown in Fig. 3K and its two vibrational modes shown in Fig. 3I, the Reynolds number is $\sim 10^2$ based on the following estimates: $\rho_{Fluid} \sim 1$ g/cm^3, $f \sim 10^3$ Hz, $L \sim 10^{-1}$ cm, and $\mu_{Fluid} \sim 10^{-2}$ Pa·s. Equation 2 is also consistent with the simulation for this double-floor rotated table structure for fluid density between 0.5 and 1.5 g/cm^3 and viscosity between 0 and 5×10^{-2} Pa·s (fig. S14). These ranges are of relevance to many biological fluids such as serum and plasma.

The scaling law serves as the basis of an inverse problem that determines the fluid density and viscosity from the resonant frequencies of the two modes, that is, the twisting mode and the piston mode. Calibration experiments involve two fluid samples with known density and viscosity (that is, water and water-glycerol mixture with 67% glycerol volume fraction), from which the constants, $K_\rho = 0.30$ and $K_\mu = 1.39$, can be obtained for the twisting mode. For the piston mode, these constants are $K_\rho = 0.088$ and $K_\mu = 0.55$. Using these values in Eq. 2 yields predicted results (Fig. 4C) that agree well with experimental data for water-glycerol mixtures with different glycerol volume fractions (for example, 20, 33, and 50%). In Fig. 4C, $\sqrt{\mu_{Fluid}}$ appears in the x axis as the Reynolds number effects on the added mass via the scaling of $Re^{-\frac{1}{2}}$. The twisting mode and the piston mode of the double-floor rotated table structure are designed specifi-

cally for their decoupled sensitivities to changes in the fluid viscosity, thereby facilitating parameter extraction. In particular, the resonant frequency is insensitive to the viscosity for the piston mode but quite sensitive for the twisting mode (Fig. 4D). This difference can be explained from the added mass. As shown in note S3, $K = K_\mu Re^{-\frac{1}{2}}/K_\rho$ measures the effect of viscosity on the added mass. Taking the resonant frequency in air as the characteristic frequency in Re, we obtain $K_{Piston}/K_{Twisting} = 0.07$, indicating that the piston mode has a much smaller effect compared to the twisting mode. The resonant frequencies of both modes are sensitive to the density (Fig. 4E). Therefore, the viscosity and density can be determined conveniently and accurately from the resonant frequencies of the two modes, as described in note S4. By comparison, a simple 2D cantilever, which represents a common design in conventional MEMS, has coupled sensitivities to both viscosity and density. As shown in Fig. 4 (F and G) and fig. S15, the resonant frequencies of both the first and the second vibration modes of the cantilever are sensitive to the fluid viscosity and density at the same time, making it difficult to determine these two properties with satisfactory accuracy. A quantitative analysis of errors in extracted fluid properties that result from uncertainties in the resonant frequencies is in note S4 and fig. S16. The maximum error in the density and viscosity determined by the 2D cantilever is roughly eight and three times larger than that determined by the 3D double-floor rotated table, respectively; the average error of the 2D cantilever is nine and three times larger than the 3D structure for density and viscosity, respectively.

Figure 4 (H and I) summarizes the calculated values of viscosity and density for the full range of water-glycerol mixtures at room temperature, with comparison to those determined with a commercial rheometer [we use a highly accurate internal flow microfluidic viscometer, which eliminates potential free surfaces artifacts for low viscosity and biological fluids; details in Materials and Methods and note S5 (54)]. The results show that both viscosity and density increase as the ratio of glycerol increases, as expected, and that the maximum discrepancy with measurements made using the rheometer is less than 5%. These results validate the scaling law and allow its use in determining viscosities and densities of other fluids, as presented in the following.

Temperature-dependent studies further demonstrate the capabilities. Figure 4J summarizes the responses in a mixture of water and glycerol (1:2) at four temperatures (24°, 31.7°, 33.7°, and 42.9°C). The twisting mode (first peak on the curve) and the piston mode (second peak) both shift to higher frequencies as the temperature increases. The temperature dependence of the shift of the twisting mode is larger than that of the piston mode. Figure 4K shows that experimental values of the resonant frequencies match well with those determined by FEA. Figure 4L presents the relative changes of the frequencies as a function of increases in temperature, illustrating that the twisting mode is more sensitive to the change in temperature than the piston mode. The viscosities calculated using the scaling law agree with those determined using the rheometer, as shown in Fig. 4M. As expected, the viscosity varies strongly with temperature, while the density varies only slightly. Collectively, the results demonstrate the utility of qualitatively distinct, well-separated modes with decoupled sensitivities to viscosity and density. The ability to tailor the geometries of the 3D structures and layouts of the PZT microactuators, guided by modeling, is critically important.

Measurements of biological, complex, and time-variant fluids
Measurement capabilities of the types outlined above have broad utility in the scientific study of complex fluids and in the engineering development

of lubricants and other fluids with industrial relevance. Viscosities of biological fluids have special significance due to their medical implications. For example, abnormally high viscosity of serum or plasma serves as a marker for various diseases, such as hyperviscosity syndrome, diabetes, cardiovascular disease, and others (55–58). Figure 5 (A and B) presents results of the double-floor rotated structure (Fig. 3K) used in phosphate-buffered saline (PBS) and cell-culturing media, respectively, along with calculated viscosities and values measured using a rheometer. The resulting dynamics exhibit separated modes, consistent with findings from the water-glycerol mixtures. The viscosities determined using the scaling law and the rheometer match to better than 8%. This is particularly significant given that traditional rheometry, for example, with a cone plate, has difficulty in measuring viscosities near that of water due to surface tension artifacts (59). Protein and

biopolymer solutions are even more difficult with traditional rheometry because of the risk of surface-active components aggregating at the fluid-air interface (60). The resonance method here avoids the free interface. In addition, the 3D device can measure both viscosity and density. Measurements of porcine serum and plasma are possible as well (Fig. 5, C and D; after filtering to remove noise by a MATLAB local regression solver based on weighted linear least squares and a second-degree polynomial model). The calculated viscosities match (to better than 10%) values obtained from the microfluidic internal flow rheometer. Measurements with the rheometer as a function of shear rate indicate that all four biological fluids show Newtonian behavior (fig. S19 and note S5).

Figure 5E presents the dynamics of 3D device in a complex, non-Newtonian fluid (Carbopol microgel particle suspension in water at pH7;
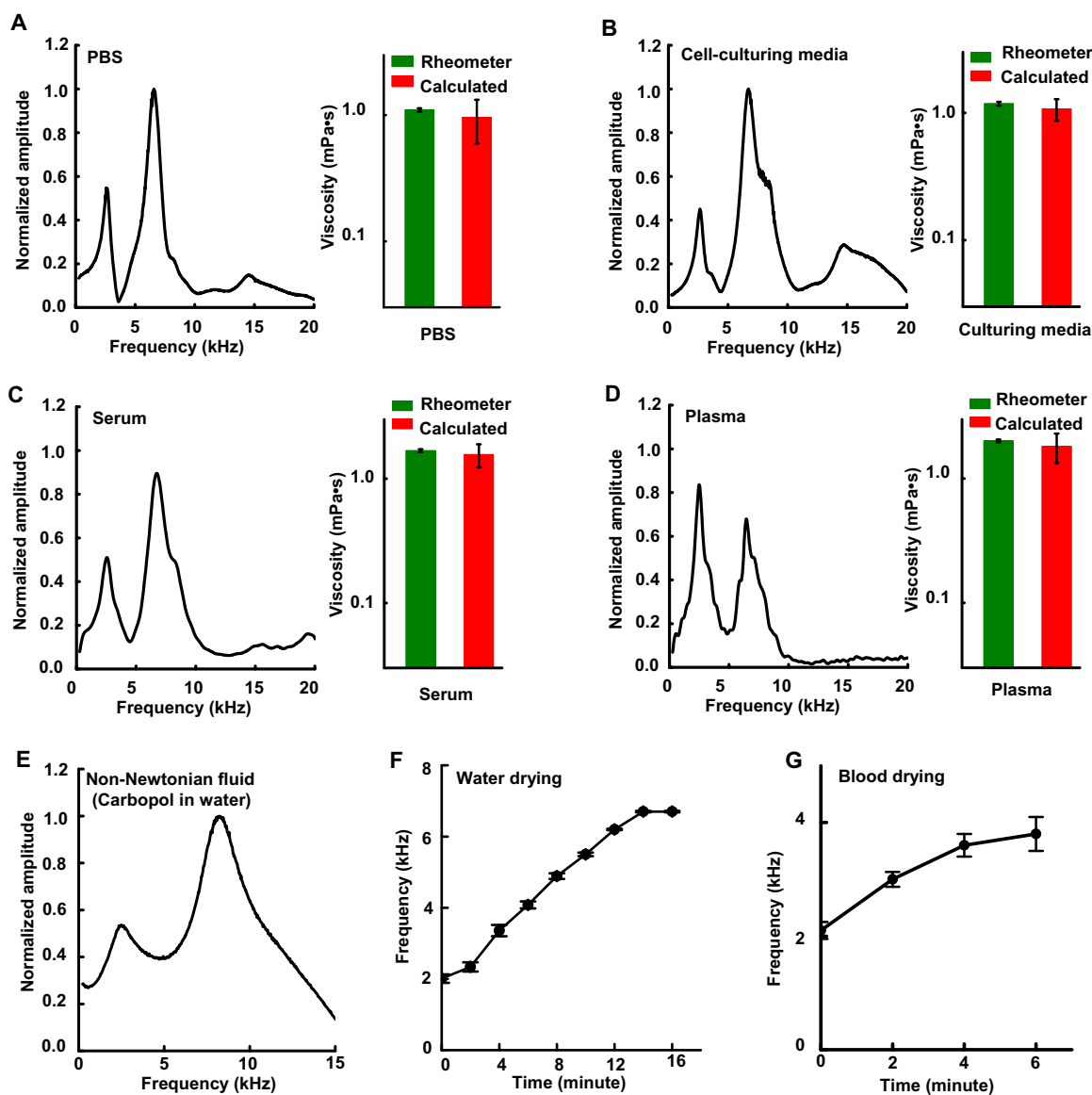

Fig. 5. Measurements of biological, complex, and time-variant fluids. (**A** to **D**) Measured vibratory responses of the double-floor rotated table in PBS, cell-culturing media, porcine serum, and porcine plasma, respectively, including the calculated viscosities and comparisons to values measured by a commercial rheometer. (**E**) Vibrational response in a complex fluid (Carbopol microgel particle suspension in water). (**F** and **G**) Change of resonant frequency of a bridge-shaped device due to the evaporation of a 5-μl droplet of water (F) and blood (G) under the device.

weight ratio, 0.065%). The high signal-to-noise ratios of these measurements illustrate potential for rheology of complex materials. The 3D systems can also serve as tools to study time-variant fluids. Figure 5 (F and G) shows that the change of the resonant frequency of a bridge-shaped device (Fig. 2A) as a 5-μl droplet of fluid (water and porcine whole blood), which is placed between the 3D device and its underlying substrate, evaporates at room temperature. The top surface of the device does not contact with the fluid, allowing the reflection of laser light from the device. Thus, capillary effects and a contact line exist in the measurement system, which changes over time during evaporation. The resonant fre-

quency increases during this process until evaporation is complete (~14 min). Similar experiments on blood show similar trends, although in this case, the resonance disappears entirely after 6 min, as a dry clot forms around the device.

Conformal integration of 3D systems on medical devices

The deformability of these 3D structures and their soft, compliant supports facilitate conformal bonding (Kwik-Sil, World Precision Instruments) onto the surfaces of medical devices and other curvilinear substrates, where they have potential as integrated sensors. Figure 6A shows a
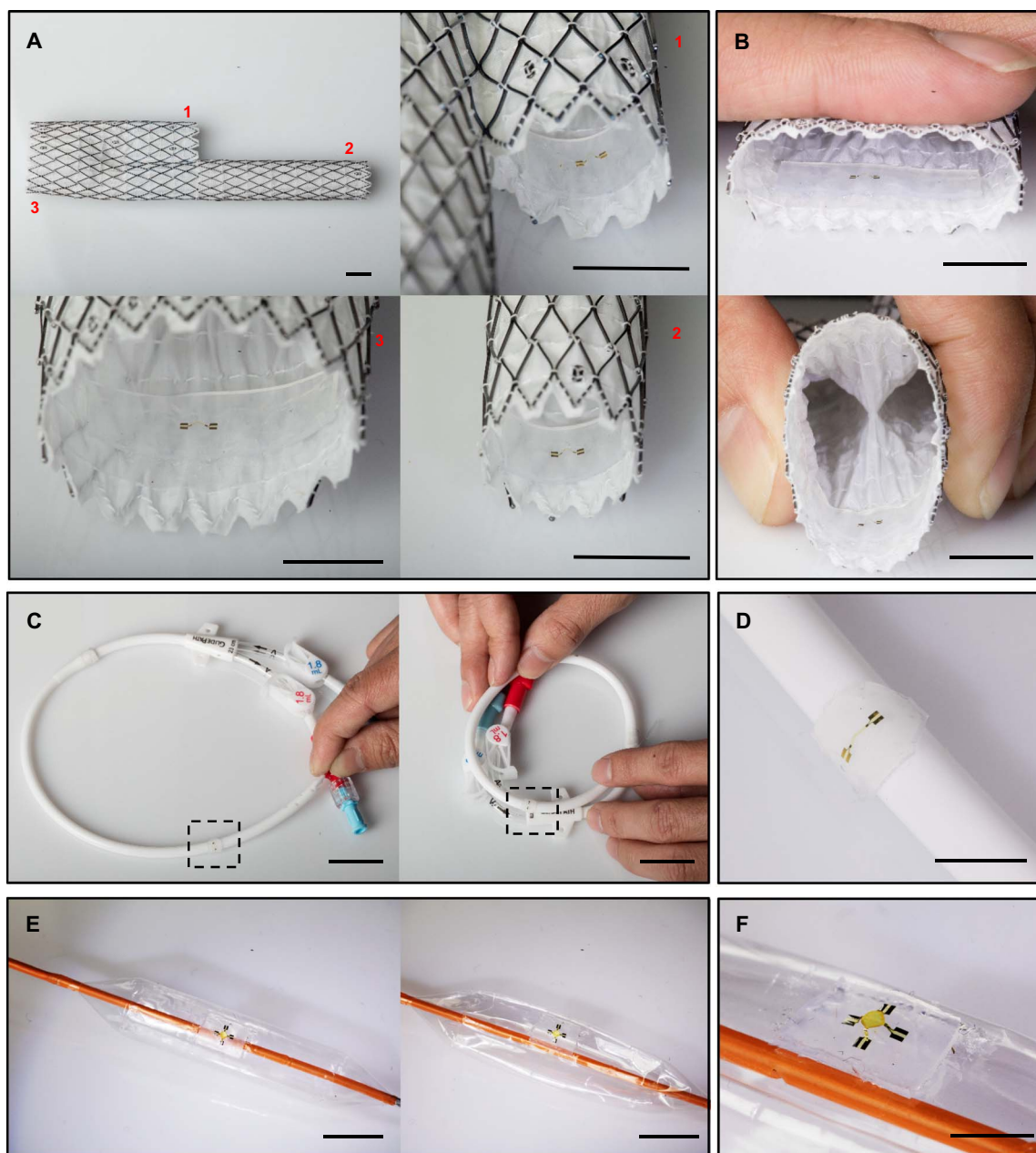
Fig. 6. Conformal integration of 3D devices onto biomedical devices. (**A**) A cardiovascular stent with three devices corresponding to tubes 1, 2, and 3, respectively. Scale bars, 1 cm. (**B**) The device deforms along with the stent while maintaining robust adhesion. Scale bar, 1 cm. (**C**) A flexible catheter with a device that is bent to different curvatures. The device is at the location of the dashed line. Scale bars, 2.5 cm. (**D**) Magnified view of a device integrated on a catheter. Scale bar, 5 mm. (**E**) A balloon catheter with a device, in an inflated (left) and deflated (right) configuration. Scale bars, 1 cm. (**F**) Magnified view of a device on the balloon. Scale bar, 5 mm.

cardiovascular stent with three devices on parts of its surface with different curvatures. This integration is robust even under the types of large deformations that occur during surgical deployment, as shown in Fig. 6B. Flexible catheters can also serve as substrates (Fig. 6, C and D). As the catheter bends into different shapes, the bonding remains intact, as shown in the magnified view of the 3D device after bending (Fig. 6D). As another example, Fig. 6E presents a 3D system (table-shaped structure) on a balloon in its inflated (left) and deflated (right) states. Figure 6F shows the close-up view.

DISCUSSION

As introduced here, capabilities for integrating functional, high-performance piezoelectric materials into complex 3D architectures create opportunities in unusual classes of systems with active, programmable mechanical function. Because the approaches are fully compatible with conventional 2D technologies, a vast collection of device types and materials are readily accessible, thereby creating avenues for extending design options in 3D MEMS and related technologies. Computational tools that can accurately capture essential aspects of the assembly processes and resulting mechanical behaviors in 3D are critically important for rapidly exploring and optimizing choices in layout and actuator configurations. Comprehensive experimental, numerical, and theoretical studies demonstrate some of the possibilities, with a focus on measuring fluid properties based on multiple 3D vibrational modes with decoupled sensitivities to viscosity and density. Validated measurements of various liquids, in microliter volumes of simple and complex materials, including biofluids, confirm the high precision associated with assembly and use of these systems. The overall results bring the full versatility of heterogeneous combinations of 2D planar technologies into the field of 3D MEMS. The implications extend beyond applications demonstrated here to include biosensing, energy harvesting, and other possibilities. The additional ability to integrate these systems onto arbitrary substrates foreshadows further opportunities for advanced sensing in clinical medicine, specifically in biomedical devices such as cardiovascular stents, catheters, and balloons.

MATERIALS AND METHODS
Preparation of PZT microactuators
Fabrication of PZT microactuators began with the formation of thin (500 nm) films of PZT (MEMS Solution Inc.) by sol-gel techniques on Pt/Ti on the oxidized surfaces of silicon wafers. Each microactuator had lateral dimensions of 200 μm × 140 μm in parallel-plate-type capacitor designs with top and bottom electrodes. Electron beam evaporation yielded a bilayer of Au/Cr (200 nm/10 nm) as the material for the top electrode on multilayers stacks of PZT/Pt/Ti/SiO$_2$ (500 nm/200 nm/5 nm/600 nm). Photolithography [photoresist (PR), AZ5214E] and wet etching (gold, TFA, Transene Company Inc.; chrome, OM Group) defined an array of top electrodes (150 μm × 100 μm; with a square notch of 50 μm × 50 μm). Additional photopatterning (mask of PR hardbaked at 150°C for 5 min) and etching [HNO$_3$ (nitric acid):BHF (buffered hydrogen fluoride):H$_2$O (deionized water) = 1:1:20] defined regions of PZT with dimensions of 180 μm × 120 μm (with a rectangle of 50 μm × 40 μm notch; for the purpose for bottom electrode connection). A final sequence of photopatterning and etching [HCl (hydrochloric acid):HNO$_3$:deionized water = 3:1:4 at 100°C through a hardbaked mask of AZ4620] defined bottom Pt/Ti electrodes

with dimensions of 200 μm × 140 μm. Next, protecting the PZT with PR (AZ4620) allowed partial undercut removal of the underlying SiO$_2$ sacrificial layer by immersion in BHF. Removing the PR with acetone allowed patterning of another layer of PR to form a top surface encapsulation and perimeter anchor to the underlying wafer. Immersion in dilute hydrofluoric acid (HF) (deionized water:49% HF = 3:1) completely removed the SiO$_2$, thereby preparing the PZT microactuators for transfer printing. Figure S1 shows the schematic illustration of the process.

PZT poling
Poling used a static electric field (200 kV cm^{-1}) at 150°C for 2 hours, applied to PZT films between the bottom and top contacts of Ti/Pt (5 nm/200 nm) and Cr/Au (10/200 nm), respectively.

Transfer printing of PZT actuators
The transfer printing process began with preparation of polydimethylsiloxane (PDMS) stamps. Photopatterning a film (100 μm thick) of a photodefinable epoxy (SU-8 100 MicroChem Corp.) on a polished silicon wafer defined an array of holes with rectangular cross sections (200 μm × 140 μm) as a mold for making the PDMS stamps. Dropcasting PDMS (Sylgard 184, Dow Corning; 10:1 ratio of prepolymer to curing agent), placing in a vacuum desiccator for 1 hour to release bubbles, and curing in an oven at 70°C for 24 hours completed the fabrication of PDMS stamps. Peeling the PDMS from the mold and mounting it on a glass slide yielded a composite structure with sufficient structural stability to facilitate transfer printing. The process of transfer printing followed the scheme in fig. S2, which used an automated tool with a digital camera and microscope system for visualization. Si wafers served as handling substrates. A layer of 40-nm-thick Cr was first deposited onto the Si wafer by electron beam deposition followed by a photolithographic process to define markers for aligning the PZT microactuators during transfer printing. Next, deposition of a film of 400-nm-thick SiO$_2$ onto the wafer by electron beam deposition yielded a sacrificial layer. Spin-casting a thin (1.2 μm) overcoat of poly(pyromellitic dianhydride-co-4,4′-oxydianiline), amic acid solution (PI) followed by baking at 90°C for 30 s provided an adhesive surface to receive the PZT microactuators at positions indicated by the markers. Baking at 150°C on a hot plate for 5 min followed by immersion into acetone removed the residual PR from the microactuators. Hardbaking the PI at 250°C in an oven for 75 min formed a robust encapsulation layer. Patterning a layer of PR and reactive ion etching (RIE; Nordson March) finally defined the geometry of this layer of PI.

Fabrication of 2D precursors
Fabrication began on the Si/Cr/SiO$_2$ wafer with transferred PZT microactuators. Spin-casting a film of PI (hardbaked at 250°C in an oven for 75 min) formed an encapsulation layer on the Au electrode side of the devices. Openings through the PI defined by RIE through a pattern of PR provided access to the metal electrode contacts. Electron beam evaporation of Au/Cr (200 nm/10 nm) on a patterned layer of PR (AZ2070) followed by immersion in acetone removed the PR to leave an array of metal interconnects. Another patterned film of PI (1.2 μm) formed an encapsulation layer over these traces. These layers of PI provided electrical insulation. Exposure to an O$_2$ plasma for 2 min ensured good adhesion between the PI and an overlayer (10 μm) of SU-8, patterned by photolithography and baked at 200°C for 20 min, with a ramp of 65°, 95°, 140°, and 180° for 1, 2, 5, and 5 min, respectively. Patterning a layer of AZ5214 (1.5 μm thick) created a sacrificial layer for the final

assembly process of 3D mesostructures. Etching the layer of SiO_2 on the surface of the wafer by immersion in diluted HF facilitated the release of 2D precursor from the wafer. Gently pressing a PDMS stamp on the wafer and then releasing it transferred the 2D precursors onto the stamp. Pressing a piece of water-soluble tape [polyvinyl alcohol (PVA)] onto the stamp and then peeling it away transferred the 2D precursors onto the tape.

Assembly of 3D mesostructures

Exposing the 2D precursors, while mounted on the PVA tape, and the prestretched silicone elastomer (0.5 mm thick; Dragon Skin, Smooth-On) to ultraviolet-induced ozone yielded hydroxyl termination on their surfaces. Laminating the PVA with precursors face down onto the silicone followed by baking in an oven at 70°C for 9 min formed strong covalent bonds between the silicone and the exposed regions of SU-8. Washing with hot water for 2 min removed the PVA tape, and immersing in acetone for 20 min dissolved the AZ5214. Slowly releasing the prestretched elastomer completed the 3D assembly process. Details appear in fig. S3 and note S6.

Measurements of vibrational modes in air and fluids

A previously developed laser system allowed measurements of frequencies of vibrational modes excited by the PZT microactuators (37). The system delivered a laser beam onto the vibrating structures. Briefly, a focusing lens and a mirror allowed a fraction of laser light scattered from the structures to be collected and delivered onto the surface of a photodetector (DET110, Thorlabs). A lock-in amplifier (SRS SR830, Stanford Research) captured the amplitude of fluctuations in the intensity of this scattered laser at certain frequencies. This signal is directly proportional to the amplitude of the vibration, across the range examined here. A signal generator (Keithley 3390) provided the driving voltage for the PZT microactuators. A LabVIEW program automatically controlled the measurement and actuation systems and captured the relevant data. Repeating the measurements 64 times at each frequency improved the signal-to-noise ratios for all experimental frequency-amplitude responses reported in this study. A PDMS chamber sealed by a pair of glass slides served to contain liquids surrounding the structures (fig. S18A). A thermal stage (fig. S18B) allowed studies at elevated-temperature resistance (MMCPH-20-15, MISUMI USA). A digital thermometer (Digi-Sense Thermometer, Davis Instrument) allowed measurements of the temperatures.

Numerical modeling

The coupled fluid-structure simulation was carried out using the commercial software ABAQUS. The shape of the buckled structure was obtained from a nonlinear postbuckling analysis. Then, a steady-state dynamic analysis enabled the calculation of the vibration mode and resonant frequency under PZT actuation. To account for the effect of the fluid on the vibration, the vibration velocity of each vibration mode was transferred to the computational fluid dynamics (CFD) analysis, which predicted the forces applied on the 3D structure by the surrounding fluids as a function of frequency. These forces were then fed back to the steady-state dynamic analysis to recalculate the resonant frequency. A Python script was developed to transfer quantities between the steady-state analysis and the CFD analysis.

Calculation of the fluid density and viscosity

On the basis of the scaling law (Eq. 2), the fluid density and viscosity were calculated by solving the following linear equations using the measured resonant frequencies of the two modes

$$C_{\rho(I)}z_1 + C_{\mu(I)}z_2 = 1 - \left(\frac{f_{\text{Fluid}}}{f_{\text{Air}}}\right)^2_{(I)} \tag{3}$$

$$C_{\rho(II)}z_1 + C_{\mu(II)}z_2 = 1 - \left(\frac{f_{\text{Fluid}}}{f_{\text{Air}}}\right)^2_{(II)} \tag{4}$$

where

$$Z_1 = \frac{L\rho_{\text{Fluid}}}{h\rho_{\text{Solid}}}, Z_2 = \left(\frac{\mu_{\text{Fluid}}\rho_{\text{Fluid}}}{h^2\rho^2_{\text{Solid}}}\right)^{\frac{1}{2}}$$

$$C_{\rho(I)} = K_{\rho(I)}\left(\frac{f_{\text{Fluid}}}{f_{\text{Air}}}\right)^2_{(I)}, C_{\mu(I)} = K_{\mu(I)}\left(\frac{f^{\frac{3}{2}}_{\text{Fluid}}}{f^2_{\text{Air}}}\right)^2_{(I)},$$

$$C_{\rho(II)} = K_{\rho(II)}\left(\frac{f_{\text{Fluid}}}{f_{\text{Air}}}\right)^2_{(II)}, C_{\mu(II)} = K_{\mu(II)}\left(\frac{f^{\frac{3}{2}}_{\text{Fluid}}}{f^2_{\text{Air}}}\right)^2_{(II)} \tag{5}$$

Measurement of viscosity using a commercial rheometer

The viscosity of the water-glycerol and biofluid samples was verified using an internal flow microfluidic microliter-sample-volume m-VROC viscometer from Rheosense Inc. Fluid was pushed through a rectangular microchannel (dimensions, 51.1 μm × 2 mm × 1.5 cm) using a syringe pump, and the pressure was measured by sensors at three points along the length of the channel. Temperature was controlled via a Thermo Cube circulator. Water-glycerol mixtures and biofluids were tested for temperature-dependent and shear rate–dependent viscosities. Additional information is in figs. S19 and S20 and note S5.

Fig. S16. Accuracy of the measured fluid density and viscosity.

Fig. S17. Measured density of the water-glycerol mixture with 66.7% glycerol volume fraction when the temperature ranges from 24° to 42.9°C.

Fig. S18. Apparatus for the measurements of vibrational modes in fluids at various temperatures.

Fig. S19. Shear rate dependence of the viscosities of the biofluids measured by the commercial rheometer, m-VROC viscometer.

Fig. S20. Schematic illustration and dimension of the fluidic channel of the commercial rheometer, m-VROC viscometer.

Movie S1. Assembly of 3D active mesostructures.

Movie S2. Vibrational modes.

REFERENCES AND NOTES

1. K. Park, L. J. Millet, N. Kim, H. Li, X. Jin, G. Popescu, N. R. Aluru, K. J. Hsia, R. Bashir, Measurement of adherent cell mass and growth. *Proc. Natl. Acad. Sci. U.S.A.* **107**, 20691–20696 (2010).

2. S. Yang, T. Saif, Micromachined force sensors for the study of cell mechanics. *Rev. Sci. Instrum.* **76**, 044301 (2005).

3. R. Jagannathan, M. T. A. Saif, MEMS sensors and microsystems for cell mechanobiology. *J. Micromech. Microeng.* **21**, 054002–054012 (2011).

4. C. Moraes, C. A. Simmons, Y. Sun, Cell mechanics meets MEMS. *CSME Bull. SCGM* 15–18 (2006).

5. M. S. Hanay, S. Kelber, A. K. Naik, D. Chi, S. Hentz, E. C. Bullard, E. Colinet, L. Duraffourg, M. L. Roukes, Single-protein nanomechanical mass spectrometry in real time. *Nat. Nano.* **7**, 602–608 (2012).

6. M. Sansa, E. Sage, E. C. Bullard, M. Gely, T. Alava, E. Colinet, A. K. Naik, L. G. Villanueva, L. Duraffourg, M. L. Roukes, Frequency fluctuations in silicon nanoresonators. arXiv:1506.08135 (2015).

7. Y.-C. Toh, C. Zhang, J. Zhang, Y. M. Khong, S. Chang, V. D. Samper, D. van Noort, D. W. Hutmacher, H. Yu, A novel 3D mammalian cell perfusion-culture system in microfluidic channels. *Lab Chip* **7**, 302–309 (2007).

8. L. Y. Yeo, H.-C. Chang, P. P. Y. Chan, J. R. Friend, Microfluidic devices for bioapplications. *Small* **7**, 12–48 (2011).

9. S. Boskovic, J. W. M. Chon, P. Mulvaney, J. E. Sader, Rheological measurements using microcantilevers. *J. Rheol.* **46**, 891–899 (2002).

10. S. Cerimovic, R. Beigelbeck, H. Antlinger, J. Schalko, B. Jakoby, F. Keplinger, Sensing viscosity and density of glycerol–water mixtures utilizing a suspended plate MEMS resonator. *Microsyst. Technol.* **18**, 1045–1056 (2012).

11. E. K. Reichel, A. Abdallah, C. Feichtenschlager, M. Kramer, A. Moritz, B. Jakoby, Viscoelasticity and dielectric measurement of small sample volume for diagnostic platform of synovial fluid. *Procedia Eng.* **120**, 171–174 (2015).

12. P. L. Green, E. Papatheou, N. D. Sims, Energy harvesting from human motion and bridge vibrations: An evaluation of current nonlinear energy harvesting solutions. *J. Intell. Mater. Syst. Struct.* **24**, 1494–1505 (2013).

13. C. Peters, D. Maurath, W. Schock, F. Mezger, Y. Manoli, A closed-loop wide-range tunable mechanical resonator for energy harvesting systems. *J. Micromech. Microeng.* **19**, 094004 (2009).

14. S. Saadon, O. Sidek, A review of vibration-based MEMS piezoelectric energy harvesters. *Energy Convers. Manag.* **52**, 500–504 (2011).

15. J. W. Judy, Microelectromechanical systems (MEMS): Fabrication, design and applications. *Smart Mater. Struct.* **10**, 1115 (2001).

16. N. S. Shaar, "Assembling 3D MEMS structures by folding, aligning and latching 2D patterned films," thesis, Massachusetts Institute of Technology (2014).

17. J. W. Gardner, V. K. Varadan, O. O. Awadelkarim, *Microsensors, MEMS, and Smart Devices* (John Wiley & Sons Ltd, 2001), vol. 1.

18. I. Dufour, A. Maali, Y. Amarouchene, C. Ayela, B. Caillard, A. Darwiche, M. Guirardel, H. Kellay, E. Lemaire, F. Mathieu, C. Pellet, D. Saya, M. Youssry, L. Nicu, A. Colin, The microcantilever: A versatile tool for measuring the rheological properties of complex fluids. *J. Sens.* **2012**, 9 (2012).

19. R. Legtenberg, A. W. Groeneveld, M. Elwenspoek, Comb-drive actuators for large displacements. *J. Micromech. Microeng.* **6**, 320–329 (1996).

20. T. L. Sounart, T. A. Michalske, K. R. Zavadil, Frequency-dependent electrostatic actuation in microfluidic MEMS. *J. Microelectromech. Syst.* **14**, 125–133 (2005).

21. A. M. Elshurafa, K. Khirallah, H. H. Tawfik, A. Emira, A. K. S. A. Aziz, S. M. Sedky, Nonlinear dynamics of spring softening and hardening in folded-MEMS comb drive resonators. *J. Microelectromech. Syst.* **20**, 943–958 (2011).

22. B. Jakoby, E. K. Reichel, F. Lucklum, B. Weiss, C. Riesch, F. Keplinger, R. Beigelbeck, W. Hilber, *Determining Liquid Properties Using Mechanically Vibrating Sensors* (Springer, 2010).

23. H. Cho, M.-F. Yu, A. F. Vakakis, L. A. Bergman, D. M. McFarland, Tunable, broadband nonlinear nanomechanical resonator. *Nano Lett.* **10**, 1793–1798 (2010).

24. S. Lee, C. Chen, V. V. Deshpande, G.-H. Lee, I. Lee, M. Lekas, A. Gondarenko, Y.-J. Yu, K. Shepard, P. Kim, J. Hone, Electrically integrated SU-8 clamped graphene drum resonators for strain engineering. *Appl. Phys. Lett.* **102**, 153101 (2013).

25. C. Chen, S. Lee, V. V. Deshpande, G.-H. Lee, M. Lekas, K. Shepard, J. Hone, Graphene mechanical oscillators with tunable frequency. *Nat. Nano.* **8**, 923–927 (2013).

26. A. W. Topol, B. K. Furman, K. W. Guarini, L. Shi, G. M. Cohen, G. F. Walker, 2004 *Proceedings 54th* in *Electronic Components and Technology Conference* (*IEEE*, 2004), vol. 1, pp. 931–938.

27. N. Miki, X. Zhang, R. Khanna, A. A. Ayón, D. Ward, S. M. Spearing, Multi-stack silicon-direct wafer bonding for 3D MEMS manufacturing. *Sensors Actuators A Phys.* **103**, 194–201 (2003).

28. T.-K. A. Chou, K. Najafi, in *Transducers '01 Eurosensors XV: The 11th International Conference on Solid-State Sensors and Actuators June 10–14, 2001 Munich, Germany*, E. Obermeier, Ed. (Springer, 2001), pp. 1542–1545.

29. S. Nihtianov, A. Luque, *Smart Sensors and MEMS: Intelligent Devices and Microsystems for Industrial Applications* (Woodhead Publishing, 2014).

30. J. Reddy, R. Pratap, Si-gold-glass hybrid wafer bond for 3D-MEMS and wafer level packaging. *J. Micromech. Microeng.* **27**, 015005 (2017).

31. C.-B. Eom, S. Trolier-McKinstry, Thin-film piezoelectric MEMS. *MRS Bull.* **37**, 1007–1017 (2012).

32. Z. Wang, J. Miao, C. W. Tan, T. Xu, Fabrication of piezoelectric MEMS devices-from thin film to bulk PZT wafer. *J. Electroceram.* **24**, 25–32 (2010).

33. B. S. Lee, S. C. Lin, W. J. Wu, X. Y. Wang, P. Z. Chang, C. K. Lee, Piezoelectric MEMS generators fabricated with an aerosol deposition PZT thin film. *J. Micromech. Microeng.* **19**, 065014 (2009).

34. S. Xu, Z. Yan, K.-I. Jang, W. Huang, H. Fu, J. Kim, Z. Wei, M. Flavin, J. McCracken, R. Wang, A. Badea, Y. Liu, D. Xiao, G. Zhou, J. Lee, H. U. Chung, H. Cheng, W. Ren, A. Banks, X. Li, U. Paik, R. G. Nuzzo, Y. Huang, Y. Zhang, J. A. Rogers, Assembly of micro/ nanomaterials into complex, three-dimensional architectures by compressive buckling. *Science* **347**, 154–159 (2015).

35. Z. Yan, F. Zhang, J. Wang, F. Liu, X. Guo, K. Nan, Q. Lin, M. Gao, D. Xiao, Y. Shi, Y. Qiu, H. Luan, J. H. Kim, Y. Wang, H. Luo, M. Han, Y. Huang, Y. Zhang, J. A. Rogers, Controlled mechanical buckling for origami-inspired construction of 3D microstructures in advanced materials. *Adv. Funct. Mater.* **26**, 2629–2639 (2016).

36. Y. Zhang, Z. Yan, K. Nan, D. Xiao, Y. Liu, H. Luan, H. Fu, X. Wang, Q. Yang, J. Wang, W. Ren, H. Si, F. Liu, L. Yang, H. Li, J. Wang, X. Guo, H. Luo, L. Wang, Y. Huang, J. A. Rogers, A mechanically driven form of Kirigami as a route to 3D mesostructures in micro/ nanomembranes. *Proc. Natl. Acad. Sci. U.S.A.* **112**, 11757–11764 (2015).

37. X. Ning, H. Wang, X. Yu, J. A. N. T. Soares, Z. Yan, K. Nan, G. Velarde, Y. Xue, R. Sun, Q. Dong, H. Luan, C. M. Lee, A. Chempakasseril, M. Han, Y. Wang, L. Li, Y. Huang, Y. Zhang, J. A. Rogers, 3D tunable, multiscale, and multistable vibrational micro-platforms assembled by compressive buckling. *Adv. Funct. Mater.* **27**, 1605914 (2017).

38. Y. Zhang, F. Zhang, Z. Yan, Q. Ma, X. Li, Y. Huang, J. A. Rogers, Printing, folding and assembly methods for forming 3D mesostructures in advanced materials. *Nat. Rev. Mater.* **2**, 17019 (2017).

39. A. Carlson, A. M. Bowen, Y. Huang, R. G. Nuzzo, J. A. Rogers, Transfer printing techniques for materials assembly and micro/nanodevice fabrication. *Adv. Mater.* **24**, 5284–5318 (2012).

40. E. Balmes, A. Deraemaeker, Modeling structures with piezoelectric materials (Theory and SDT Tutorial, 2013).

41. O. Guillon, F. Thiebaud, D. Perreux, Tensile fracture of soft and hard PZT. *Int. J. Fract.* **117**, 235–246 (2002).

42. H. Cao, A. G. Evans, Nonlinear deformation of ferroelectric ceramics. *J. Am. Ceram. Soc.* **76**, 890–896 (1993).

43. M. Youssry, N. Belmiloud, B. Caillard, C. Ayela, C. Pellet, I. Dufour, A straightforward determination of fluid viscosity and density using microcantilevers: From experimental data to analytical expressions. *Sensors Actuators A Phys.* **172**, 40–46 (2011).

44. L. R. A. Follens, E. K. Reichel, C. Riesch, J. Vermant, J. A. Martens, C. E. A. Kirschhock, B. Jakoby, Viscosity sensing in heated alkaline zeolite synthesis media. *Phys. Chem. Chem. Phys.* **11**, 2854–2857 (2009).

45. E. Lemaire, M. Heinisch, B. Caillard, B. Jakoby, I. Dufour, in *13th Mechatronics International Conference* (Institute for Microelectronics and Microsensors, Johannes Kepler Univ., Linz, Austria, 2012), 5 pp.

46. M. Heinisch, T. Voglhuber-Brunnmaier, E. K. Reichel, I. Dufour, B. Jakoby, Electromagnetically driven torsional resonators for viscosity and mass density sensing applications. *Sensors Actuators A Phys.* **229**, 182–191 (2015).

47. B. Jakoby, in *2015 Transducers - 2015 18th International Conference on Solid-State Sensors, Actuators and Microsystems* (*TRANSDUCERS*), pp. 686–691.

48. M. Heinisch, E. K. Reichel, T. Voglhuber-Brunnmaier, B. Jakoby, in *2012 IEEE Sensors* (2012), pp. 1–4.

49. E. K. Reichel, M. Heinisch, B. Jakoby, J. Vermant, C. E. A. Kirschhock, in *2012 IEEE Sensors* (2012), pp. 1–4.

50. N. Belmiloud, I. Dufour, A. Colin, L. Nicu, Rheological behavior probed by vibrating microcantilevers. *Appl. Phys. Lett.* **92**, 041907 (2008).

51. B. Weiss, M. Heinisch, B. Jakoby, E. K. Reichel, in *2011 IEEE Sensors Proceedings* (IEEE, 2011), pp. 1538–1541.

52. B. Ilic, S. Krylov, H. G. Craighead, Young's modulus and density measurements of thin atomic layer deposited films using resonant nanomechanics. *J. Appl. Phys.* **108**, 044317 (2010).

53. J. E. Sader, Frequency response of cantilever beams immersed in viscous fluids with applications to the atomic force microscope. *J. Appl. Phys.* **84**, 64–76 (1998).

54. *RheoSense* (2016); www.rheosense.com/products/viscometers/m-vroc/how-it-works.

55. U. Windberger, A. Bartholovitsch, R. Plasenzotti, K. J. Korak, G. Heinze, Whole blood viscosity, plasma viscosity and erythrocyte aggregation in nine mammalian species: Reference values and comparison of data. *Exp. Physiol.* **88**, 431–440 (2003).

56. N. K. Howell, R. A. Lawrie, Functional aspects of blood plasma proteins. *Int. J. Food Sci. Technol.* **22**, 145–151 (1987).

57. L. Pedersen, E. B. Nielsen, M. K. Christensen, M. Buchwald, M. Nybo, Measurement of plasma viscosity by free oscillation rheometry: Imprecision, sample stability and establishment of a new reference range. *Ann. Clin. Biochem.* **51**, 495–498 (2013).

58. G. Késmárky, P. Kenyeres, M. Rábai, K. Tóth, Plasma viscosity: A forgotten variable. *Clin. Hemorheol. Microcirc.* **39**, 243–246 (2008).

59. M. T. Johnston, R. H. Ewoldt, Precision rheometry: Surface tension effects on low-torque measurements in rotational rheometers. *J. Rheol.* **57**, 1515–1532 (2013).

60. V. Sharma, A. Jaishankar, Y.-C. Wang, G. H. McKinley, Rheology of globular proteins: Apparent yield stress, high shear rate viscosity and interfacial viscoelasticity of bovine serum albumin solutions. *Soft Matter* **7**, 5150–5160 (2011).

Citation: X. Ning, X. Yu, H. Wang, R. Sun, R. E. Corman, H. Li, C. M. Lee, Y. Xue, A. Chempakasseril, Y. Yao, Z. Zhang, H. Luan, Z. Wang, W. Xia, X. Feng, R. H. Ewoldt, Y. Huang, Y. Zhang, J. A. Rogers, Mechanically active materials in three-dimensional mesostructures. *Sci. Adv.* **4**, eaat8313 (2018).

Science Advances

Mechanically active materials in three-dimensional mesostructures

Xin Ning, Xinge Yu, Heling Wang, Rujie Sun, R. E. Corman, Haibo Li, Chan Mi Lee, Yeguang Xue, Aditya Chempakasseril, Yao Yao, Ziqi Zhang, Haiwen Luan, Zizheng Wang, Wei Xia, Xue Feng, Randy H. Ewoldt, Yonggang Huang, Yihui Zhang and John A. Rogers

ARTICLE TOOLS	http://advances.sciencemag.org/content/4/9/eaat8313
SUPPLEMENTARY MATERIALS	http://advances.sciencemag.org/content/suppl/2018/09/10/4.9.eaat8313.DC1
REFERENCES	This article cites 45 articles, 3 of which you can access for free http://advances.sciencemag.org/content/4/9/eaat8313#BIBL
PERMISSIONS	http://www.sciencemag.org/help/reprints-and-permissions

Use of this article is subject to the Terms of Service